RSC Advances

PAPER

View Article Online
View Journal | View Issue

Cite this: *RSC Adv.*, 2025, **15**, 25041

Hierarchical porous adsorbent from asphaltenes fibers and its application for methyl orange removal†

Hiyam Khalil, [a] Amgad Salama, *[bc] TriDung Ngo,[d] Thomas Kaminski[d] and Maen M. Husein *[a]

Received 1st May 2025
Accepted 9th July 2025

DOI: 10.1039/d5ra03061g

rsc.li/rsc-advances

This study explores the preparation of hierarchical porous adsorbent starting from asphaltenes fibers. Solid or aqueous KOH, $Fe(NO_3)_3$, and $Al(NO_3)_3$ activation agents were mixed with the fibers followed by treatment at 573 K for 24 h under air atmosphere. The resulting structures were characterized and assessed as adsorbents for methyl orange from aqueous solutions. Asphaltenes fibers modified with solid $Al(NO_3)_3$ exhibited the highest adsorption capacity (6.32 mg g^{-1}) and removal efficiency (79%) at 298 K and pH = 3. The intraparticle diffusion kinetic model fitted the experimental data across two time zones corresponding to initial diffusion into the mesopores followed by diffusion into micropores. The second zone could equally be modeled by a pseudo-second order model corresponding to chemisorption onto active sites. The equilibrium uptake was best described by Langmuir isotherm, indicating monolayer chemisorption of endothermic nature (ΔH^0 = 8.41 kJ mol^{-1}). The modified fibers retained significant adsorption capacity with 76.22% of initial adsorption capacity over five cycles, demonstrating their stability and reusability. This study highlights the potential of chemically activated asphaltenes fibers as effective adsorbents for wastewater treatment.

1. Introduction

The quality of natural waters is increasingly compromised by calcitrant pollutants from industrial, agricultural, and domestic sources. Contaminants such as heavy metals and organic compounds that pose serious health and environmental risks[1] continue to find their way into the different water bodies. Methyl orange (MO) is a synthetic organic azo dye widely used in textiles, printing, and as a pH indicator.[2] MO wide use, resistance to biodegradation as well as its potential toxicity to aquatic ecosystems make it a significant water contamination.[3]

Among the different water treatment methods, adsorption has proven highly effective due to its adaptability and affordability. The performance of the adsorption process depends largely on the adsorbent material, which must effectively capture pollutants and contribute to no or little back contamination.[4,5] Carbon-based adsorbents, including graphene oxide (GO), carbon nanotubes (CNTs), and activated carbon, are widely used due to their high surface area, stability, and reusability. However, materials such as GO and CNTs are relatively costly and can complicate post-treatment due to their nanoscale size and mechanical stability, raising additional environmental concerns.[6] As a result, there is a growing need to develop cost-effective, reusable, and eco-friendly adsorbents for sustainable water treatment.

Asphaltenes particles, a by-product of the petroleum industry, present a promising alternative. Asphaltenes are abundant, inexpensive, and can be chemically modified. Asphaltenes pose challenges during oil production and processing, leading to significant losses.[7] On the other hand, the use of asphaltenes particles as adsorbents has been successfully demonstrated, especially when chemically activated with KOH. KOH-activated asphaltenes particles exhibited remarkable adsorption for CO_2 (7.15 mmol g^{-1}) and H_2S (12.86 mmol g^{-1}) under atmospheric pressure at 298 K, alongside a stable cyclic adsorption–desorption performance.[8] Moreover, asphaltenes particles mixed with KOH in a 1 : 2 mass ratio and heated to 873 K displayed high surface area (970 m^2 g^{-1}) and significant adsorption for methylene blue (218.15 mg g^{-1}).[9] Nevertheless, KOH activation has some drawbacks, including the corrosiveness of KOH, which requires careful handling and disposal.[10] The alkaline by-products from KOH activation must be neutralized before disposal.[10] In addition, excessive KOH reactivity may damage the carbon structure.[11] Alternative activation

[a]*Department of Chemical & Petroleum Engineering, University of Calgary, Calgary, AB, T2N 1N4, Canada. E-mail: mhusein@ucalgary.ca*

[b]*Department of Mechanical Engineering, University of Saskatchewan, Saskatoon, SK, S7N 5A9, Canada. E-mail: amgad.salama@uregina.ca*

[c]*Department of Mechanical and Aerospace Engineering, Nazarbayev University, Astana 010000, Kazakhstan*

[d]*Energy Services, InnoTech Alberta, Edmonton, AB, Canada*

† Electronic supplementary information (ESI) available. See DOI: https://doi.org/10.1039/d5ra03061g

agents such as $Fe(NO_3)_3$ and $Al(NO_3)_3$ address these shortcomings and proved effective at creating porous structures. For example, iron-containing carbon foam (Fe-CF) with hierarchical porous structure was synthesized by first carbonizing a mixture of epoxy resin and nano-magnesium oxide, followed by $Fe(NO_3)_3$ activation.[12] Hierarchical porous carbon was also created using glucose and $Fe(NO_3)_3 \cdot 9H_2O$ in $ZnCl_2$–KCl molten salt.[13] The impact of different amounts of $Fe(NO_3)_3 \cdot 9H_2O$ on the surface area and adsorption capabilities for methylene blue and methyl orange was examined.[13] Lastly, $Al(NO_3)_3$ activation contributed to stable hierarchical micropores and mesopores structure on zeolite.[14]

Asphaltenes fibers offer significant handling advantages over asphaltenes particles due to their larger size and fibrous structure, which make them easier to separate from treated water, hence reducing back contamination. Asphaltenes fibers robustness also allows for multiple reuse cycles, contributing to cost-effectiveness.[15] While KOH activation of asphaltenes-based carbon fibers has been studied,[16] $Fe(NO_3)_3$ and $Al(NO_3)_3$ activation has not been explored. This study explores the use of $Fe(NO_3)_3$ and $Al(NO_3)_3$ as activation agents and aims at establishing hierarchical porous carbons (HPCs) starting from asphaltenes fibers. KOH activation is compared, together with the solid and wet impregnation techniques. MO removal from aqueous solution was used to assess the performance of the hierarchical adsorbent, and adsorption isotherms and kinetics were established.

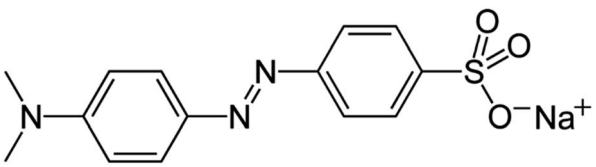

Fig. 1 Chemical structure of MO.

2. Experimental methods

2.1. Asphaltenes fibers modification

The as-received asphaltenes fibers (AsphF) used in this study was provided by InnoTech Alberta (Edmonton, AB, Canada). MO has a chemical formula of $C_{14}H_{14}N_3NaO_3S$ and molar mass of 327.33 g mol^{-1} (85% pure, ACS, Canada). The chemical structure of MO is shown in Fig. 1. Chemical reagents such as KOH (≥85% pure), $Fe(NO_3)_3 \cdot 9H_2O$ (≥98% pure), and $Al(NO_3)_3 \cdot 9H_2O$ (≥98% pure) were all obtained from Sigma-Aldrich (Canada) and used as received. Double-distilled water was used for all experiments.

Solid or aqueous solution of KOH, $Fe(NO_3)_3 \cdot 9H_2O$, or $Al(NO_3)_3 \cdot 9H_2O$ is used to synthesize chemically activated AsphF following Scheme 1. The AsphF are mixed with the different reagents at 1 g fiber : 2 g reagent using solid mixing or impregnation. Impregnation involves dissolving 0.6 g of the chemical reagent in 10 mL of water before mixing with AsphF. The mixture is then placed in an oven at 573 K for 24 h under air atmosphere. The activated AsphF were collected and left to cool to room temperature naturally. The fibers are then washed with distilled water to ensure a neutral pH and left to dry in the oven at 343 K for 3 h. Control samples exposed only to the heat treatment step were collected for comparison.

The modified samples were given short names as follows: AsphF-T for the heat-treated sample without chemicals; AsphF/KOHs-T and AsphF/KOHaq-T for samples treated with solid and

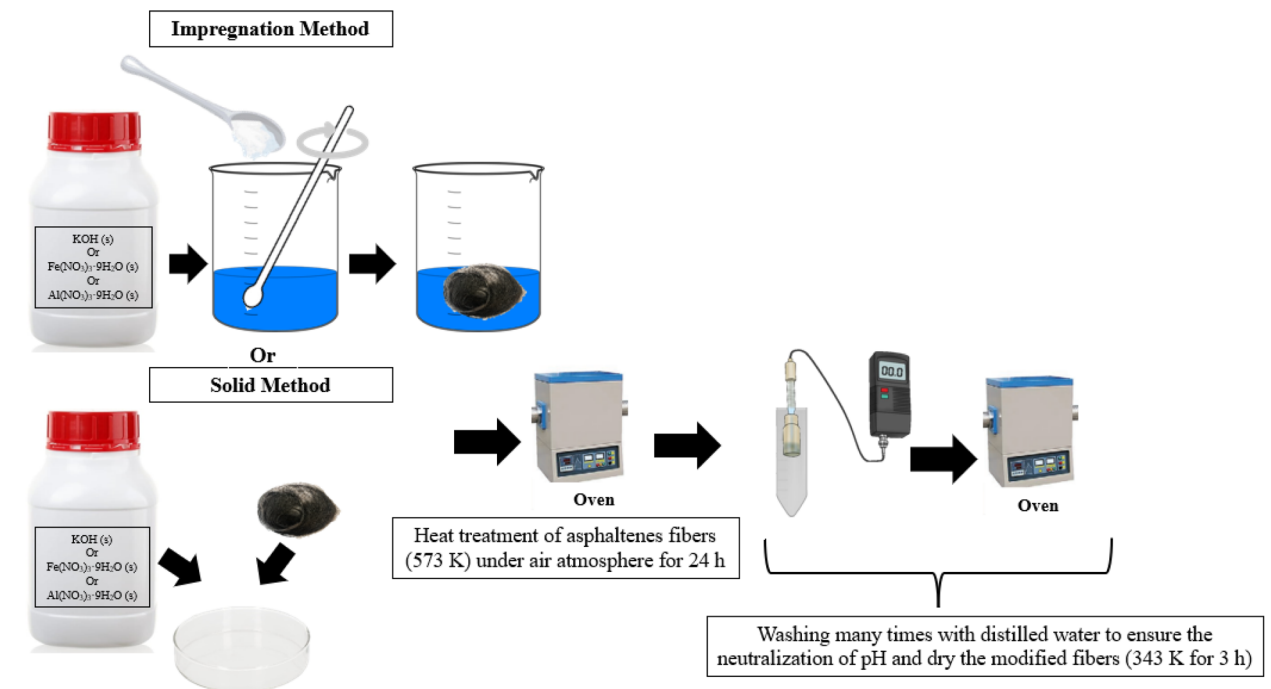

Scheme 1 The synthesis steps of different chemically activated AsphF.

aqueous KOH; AsphF/$Fe(NO_3)_3$s-T and AsphF/$Fe(NO_3)_3$aq-T for samples treated with solid and aqueous $Fe(NO_3)_3$; and AsphF/$Al(NO_3)_3$s-T and AsphF/$Al(NO_3)_3$aq-T for samples treated with solid and aqueous $Al(NO_3)_3$. These names are also explained in the Abbreviations section.

The preparation of chemically activated AsphF potentially offers a cost-effective strategy for developing functional adsorbents suitable for water treatment applications. Asphaltenes are an abundant and low-cost byproduct of the petroleum industry.[7] The activating agents used in this work, including KOH, $Fe(NO_3)_3$, and $Al(NO_3)_3$, are widely available and reasonably priced.[17–19] The thermal activation process relies on heating in air, which helps reduce operational complexity and energy requirements. We note that the preparation of asphaltenes fibers through electrospinning has also been reported as cost-effective, with the raw asphaltenes valued at approximately $0.04 USD per kg.[20] A recent techno-economic analysis further indicates that the production cost of asphaltenes-based carbon fibers can be kept below $9 USD per kg.[21] Asphaltenes fibers could be less expensive in comparison with some conventional carbon fiber precursors such as polyacrylonitrile (PAN), which typically cost ~$25 USD per kg.[21] These economic and material advantages support the feasibility of using asphaltene-based adsorbents in large-scale water treatment systems, especially where affordability and material availability are key considerations.

2.2. Modified AsphF characterization tests

The morphology of the modified AsphF was examined using scanning electron microscopy (SEM) (Phenom, Thermo Fisher Scientific, USA) operating at 15 kV accelerating voltage under low vacuum of 50 Pa. Elemental composition of carbon and oxygen for the untreated and chemically treated AsphF was studied using energy-dispersive X-ray spectroscopy (EDX) analysis was performed with Phenom, Thermo Fisher Scientific (USA). Nitrogen adsorption/desorption isotherms were established using a Gemini VII 2390 surface area analyzer (Micromeritics, USA) at 77 K after degassing the samples in N_2 environment at 393 K for 24 h. The specific surface area and pore size distribution of the asphaltenes samples were calculated using the adsorption/desorption isotherms of N_2 at 77 K using the multi-point Brunauer–Emmett–Teller (BET) and Barrett–Joyner–Halenda (BJH) equations. Additionally, Fourier-transform infrared spectroscopy (FTIR) was performed on an Agilent Cary 630 spectrometer (Agilent, USA) over a wavelength range of 650–4000 cm^{-1}. Each sample was scanned 64 times to identify the functional groups.

2.3. Batch adsorption experiments

Batch adsorption experiments were carried out in an incubator shaker (Orbital Shaker – Incubator ES-20, Grant-bio, Canada) to assess the effectiveness of the AsphF in adsorbing MO before and after modification. The effect of solution pH (3 to 11) and temperature (298 K, 313 K, and 333 K) on the adsorption was evaluated. Detailed conditions for the batch adsorption experiments are summarized in Table 1.

To investigate the performance of the different adsorbents, a specified amount of the modified/unmodified AsphF was mixed with 10 mL of 20 mg per L MO solution to achieve 2.5 g L^{-1} adsorbent dosage at pH ~ 7.0, 200 rpm and 298 K. Preliminary tests from the kinetics study showed that MO adsorption after 24 h is sufficiently close to equilibrium, while still preserving the chemistry of the mixture from external variable, *e.g.* CO_2 dissolution. The modified AsphF with the optimal adsorption performance; namely AsphF/$Al(NO_3)_3$s-T, was selected to carry out further studies. Detailed kinetics study was conducted by varying contact time 0–72 h at 298 K, 2.5 g L^{-1} adsorbent, and pH ~ 7.0 for MO initial concentrations, C_i, of 20, 25, and 30 mg L^{-1}. The adsorption isotherms were established by varying C_i between 5–30 mg L^{-1} and the thermodynamic parameters were obtained for 298 K, 313 K, and 333 K at pH ~ 7.0. The effect of solution pH on MO removal was examined within a pH range of 3–11 at 298 K, 2.5 g L^{-1} adsorbent, and $C_i = 20$ mg L^{-1}. The pH was adjusted as needed with 0.1 M HCl or 0.1 M NaOH solution and was measured by pH meter (Mettler Toledo Biotechnology S210, Canada). MO concentration was determined by measuring its maximum absorbance at $\lambda_{max} = 464$ nm using UV-vis spectrophotometer (Shimadzu, model UV-2600, Japan). A calibration curve correlating absorbance at 464 nm with MO concentration (1.25–35 mg L^{-1}) was establish based on Beer–Lambert law.[21] Doubled distilled water was used as a blank. MO uptake by modified/unmodified AsphF at a given time, q_t (mg g^{-1}), and the percent removal (%) of MO were calculated per eqn (1) and (2), respectively.

$$q_t = \frac{(C_i - C_t)V}{m} \quad (1)$$

$$\text{Removal } (\%) = \frac{(C_i - C_t)}{C_i} \times 100 \quad (2)$$

Since relatively low concentration of MO was used, the solution volume in eqn (1) is assumed to be time independent. At equilibrium, q_t and C_t are replaced with the equilibrium uptake

Table 1 Batch adsorption experimental parameters

Study	Adsorbent	C_i (mg L^{-1})	t (h)	T (K)	pH
Adsorption performance	Modified/unmodified AsphF included in this study	20	24	298	7
Kinetics	AsphF/$Al(NO_3)_3$s-T	20–30	0–72	298	7
Isotherms	AsphF/$Al(NO_3)_3$s-T	5–30	24	298–333	7
Thermodynamics	AsphF/$Al(NO_3)_3$s-T	20	24	298–333	7
Impact of pH	AsphF/$Al(NO_3)_3$s-T	20	24	298	3–11

Table 2 Kinetics models, isotherms and thermodynamic relations used to describe the adsorption of MO onto AsphF/Al$(NO_3)_3$s-T

Kinetic model (rate equation)	Integral equation	Equation number	Reference
Pseudo-first order	$q_t = q_e(1 - e^{-k_1 t})$	(3)	22
	$\log(q_e - q_t) = \log q_e - \frac{k_1}{2.303} t$	(4)	
Pseudo-second order	$q_t = \frac{{q_e}^2 k_2 t}{q_e k_2 t + 1}$	(5)	
	$\frac{t}{q_t} = \frac{1}{k_2 {q_e}^2} + \frac{1}{q_e} t$	(6)	
Elovich	$q_t = \left(\frac{1}{\beta}\right)\ln(\alpha\beta) + \left(\frac{1}{\beta}\right)\ln t$	(7)	
Intraparticle diffusion	$q_t = k_i t^{\frac{1}{2}} + I$	(8)	
Bangham	$\log\left(\frac{C_i}{C_i - q_t m}\right) = \log\left(\frac{k_0 m}{2.303 V}\right) + \alpha \log(t)$	(9)	
Isotherm models			
Langmuir	$\frac{C_e}{q_e} = \frac{1}{q_{max\text{-}L} K_L} + \frac{C_e}{q_{max\text{-}L}}$	(10)	23
	$R_L = \frac{1}{1 + K_L C_i}$	(11)	
Freundlich	$\ln q_e = \ln K_F + \frac{1}{n} \ln C_e$	(12)	
Temkin	$q_e = B \ln A + B \ln C_e$	(13)	
	$B = \frac{R T}{b_T}$	(14)	
Dubinin–Radushkevich (D–R)	$\ln q_e = \ln q_{max\text{-}D\text{-}R} - \beta\varepsilon^2$	(15)	
	$\varepsilon = RT \ln\left(1 + \frac{1}{C_e}\right)$	(16)	
	$E = \frac{1}{\sqrt{2\beta}}$	(17)	
Thermodynamic relation			
	$\ln K = \left(\frac{\Delta S^0}{R}\right) - \left(\frac{\Delta H^0}{RT}\right)$	(18)	24
	$K = K_L \times 1000 \times M \times C^0$	(19)	
	$\Delta G^0 = -RT \ln K$	(20)	

(q_e, mg g^{-1}) and the equilibrium concentration (C_e, mg L^{-1}). The equations used to analyze adsorption kinetics, isotherms, and thermodynamic properties are summarized in Table 2.

2.4. Adsorbent regeneration

To evaluate the reusability of the adsorbents, regeneration tests were conducted. The tests involved mixing 2.5 g per L AsphF/Al$(NO_3)_3$s-T with 10 mL of 20 mg per L MO solution at pH = 7 at room temperature. Following equilibrium, the adsorbent was recovered using Whatman filter paper (no. 1, 11 μm), mixed into 20 mL ethanol for 1 h at 298 K, then washed repeatedly with distilled water to remove residual MO or ethanol. After washing, the regenerated adsorbent was dried at 343 K for 3 h and reused.

3. Results and discussion

3.1. Characterization of the modified AsphF

The SEM images in Fig. 2 and S1† capture the structural changes in AsphF under various treatment conditions. The control samples (AsphF and AsphF/W) in Fig. 2a and S1a† depict a destroyed structure likely due to thermal stress/hydrolysis during heat treatment at 573 K under air atmosphere. Fig. 2b shows the samples treated with KOH, where solid mixing resulted in the formation of small pores, whereas the impregnation method caused significant destruction of the fiber structure. Fig. 2c and S1c† reveal that both solid $Al(NO_3)_3 \cdot 9H_2O$ mixing and impregnation produced pores; nevertheless, solid mixing generated larger and more abundant pores. Similarly, the samples treated with solid and aqueous $Fe(NO_3)_3 \cdot 9H_2O$ in Fig. 2d and S1d,† respectively, depict the formation of pores and ash in both treatments. Again, solid mixing exhibits a higher extent of pores and a more preserved structure which qualifies as hierarchical structure. Furthermore, the intact nature of the product and the ease of separating the fibers after treatment highlight the structural integrity achieved through solid mixing. These observations underscore the effectiveness of activating AsphF using solid mixing in preserving fiber structure and increasing porosity, rendering it a superior method compared to impregnation. Therefore, the rest of the characterization tests were performed on samples modified by solid mixing. The oxidizing agents $Al(NO_3)_3 \cdot 9H_2O$ and $Fe(NO_3)_3 \cdot 9H_2O$ help in conserving the

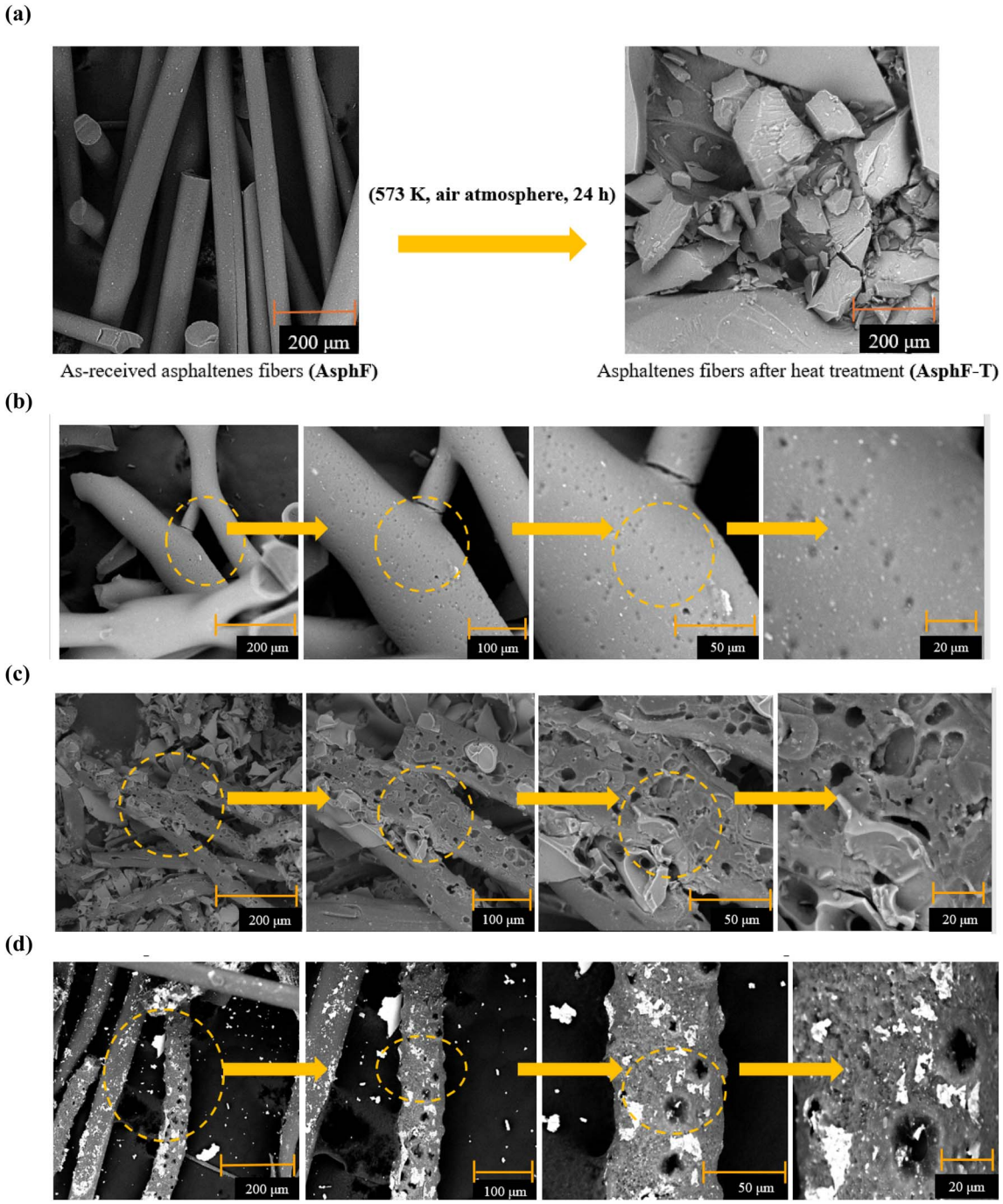

Fig. 2 SEM images of AsphF with and without solid activation under air atmosphere at 573 K for 24 h: (a) AsphF and AsphF-T (b) AsphF/KOHs-T (c) AsphF/Al$(NO_3)_3$s-T (d) AsphF/Fe$(NO_3)_3$s-T.

structure of AsphF during heat treatment by virtue of NO_3^- (nitrate ions). Nitrate ions act as mild oxidizing agents, facilitating controlled oxidation away from excessive degradation or fragmentation of the fiber structure, while incorporating oxygen-containing functional groups. This explanation draws from previous research on acid oxidizing agents, *e.g.* HNO_3, to stabilize asphaltenes-derived carbon fibers.[25]

Activation time is also one of the factors that affect the morphology of AsphF.[26] As the activation time increased, the surface of the AsphF became rougher, as evident in the SEM images of Fig. S2.†

The hierarchical porous structures in Fig. 2 dictated the nitrogen adsorption–desorption isotherms in Fig. 3. The untreated AsphF exhibit minimal nitrogen adsorption, suggesting very low porosity, while chemically modified fibers, especially AsphF/KOHs-T, AsphF/Fe$(NO_3)_3$s-T, and AsphF/Al$(NO_3)_3$s-T, displayed significant adsorption and distinct hysteresis loops, confirming the presence of mesopores.[27] The

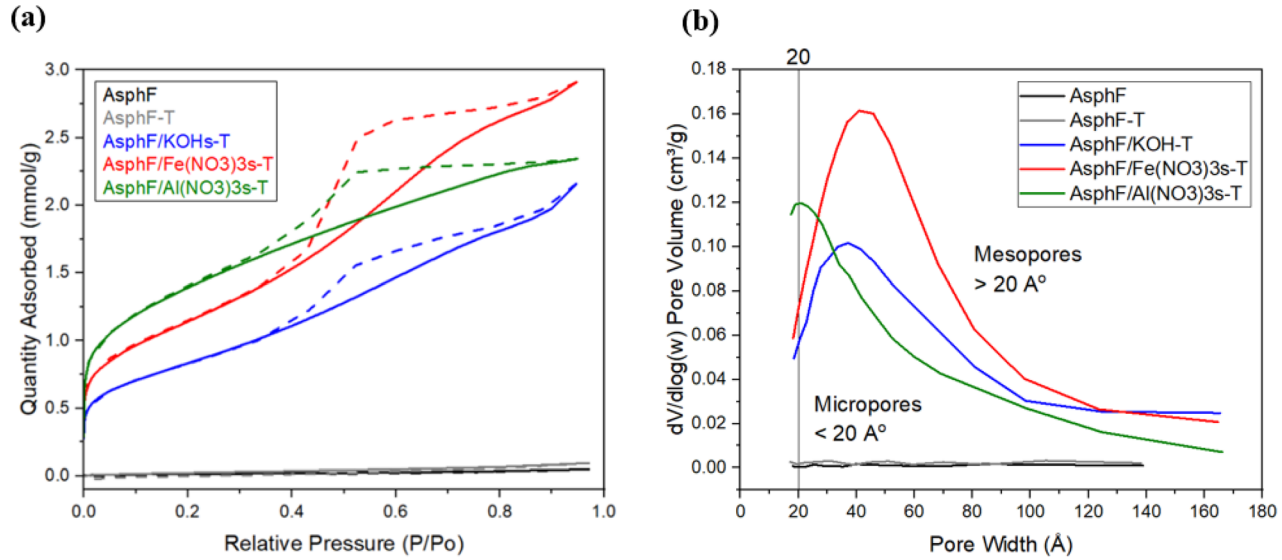

Fig. 3 (a) Nitrogen adsorption–desorption isotherms of the modified and unmodified AsphF (dashed lines indicate desorption); (b) pore size distribution.

pore size distribution for the chemically modified fibers in Table 3 showed substantial mesopores (30–50 Å) volume (V_{meso}) of range 0.075–0.101 $cm^3\ g^{-1}$ with a small contribution from micropores (<20 Å) volume (V_{micro}) of range 0.0004–0.00009 $cm^3\ g^{-1}$. The untreated AsphF show the lowest specific surface area (S_{BET}) of 1.27 $m^2\ g^{-1}$ and minimal total pore volume (V_{total}). AsphF-T exhibit a slight increase in S_{BET} (2.12 $m^2\ g^{-1}$) and pore volumes. Significantly enhanced properties are observed in AsphF/KOHs-T showing an S_{BET} of 66.57 $m^2\ g^{-1}$ and a notable increase in mesopore volume (0.075 $cm^3\ g^{-1}$). The highest surface area is achieved with AsphF/$Al(NO_3)_3$s-T and AsphF/$Fe(NO_3)_3$s-T, with S_{BET} values of 110.2 $m^2\ g^{-1}$ and 91.80 $m^2\ g^{-1}$, respectively, and corresponding increase in V_{total} and V_{meso}. These results suggest that $Fe(NO_3)_3$ and $Al(NO_3)_3$ are superior chemical activation agents to the more widely used KOH.

The FTIR spectra in Fig. 4 display the structural changes in untreated and chemically modified asphaltenes fibers. For AsphF, peaks at 2922 cm^{-1} and 2847 cm^{-1} correspond to the asymmetric and symmetric stretching vibrations of aliphatic C–H bonds, indicating the presence of long aliphatic chains.[28,29] The peak at 2105 cm^{-1} suggests the presence of weak C≡C stretching vibrations or carbonaceous materials, which are

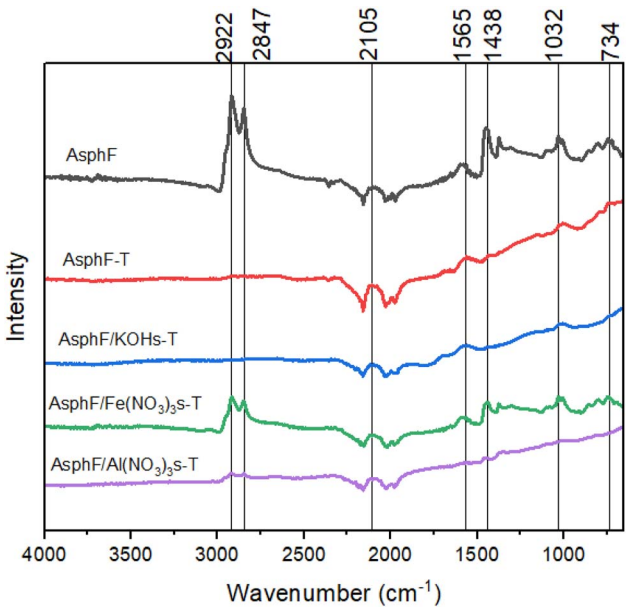

Fig. 4 FTIR spectra of AsphF before and after chemical modification.

Table 3 Specific surface area, micropore and mesopore volume of the modified and unmodified AsphF obtained from N_2 adsorption–desorption isotherms at 77 K

	Type of isotherm	S_{BET}[a] ($m^2\ g^{-1}$)	V_{total}[b,e] ($cm^3\ g^{-1}$)	V_{micro}[c] ($cm^3\ g^{-1}$)	V_{meso}[d] ($cm^3\ g^{-1}$)
AsphF	I	1.27	0.002	0.002	N/D[f]
AsphF-T	I	1.94	0.003	0.003	N/D[f]
AsphF/KOHs-T	IV	66.57	0.075	0.0004	0.075
AsphF/$Al(NO_3)_3$s-T	IV	110.2	0.081	0.0053	0.076
AsphF/$Fe(NO_3)_3$s-T	IV	91.80	0.101	0.00009	0.101

[a] S_{BET} = specific surface area based on BET. [b] V_{total} = total pore volume at $P/P_o \sim 0.99$. [c] V_{micro} = T-plot micropore volume. [d] $V_{meso} = V_{total} - V_{micro}$. [e] Cumulative volume of pores using BJH method. [f] N/D = not determined.

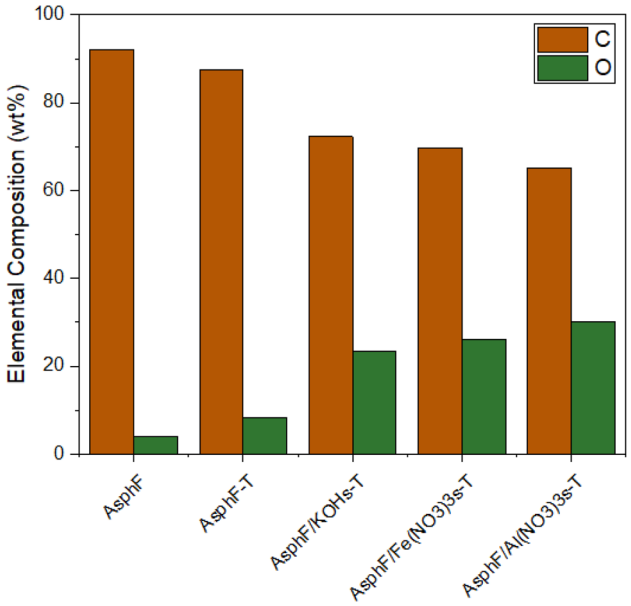

Fig. 5 Elemental composition of carbon (C) and oxygen (O) for the untreated and chemically treated AsphF.

common in asphaltenes structures.[30] The band at 1565 cm^{-1} is attributed to the stretching vibrations of aromatic C=C bonds, confirming the aromatic nature of asphaltenes.[29,31] The peak at 1438 cm^{-1} corresponds to aliphatic C–H bending vibrations, further validating the presence of aliphatic hydrocarbons.[29] The peak at 1032 cm^{-1} can be attributed to the ester linkages found in the asphaltenes molecule.[32] For the modified AsphF, distinct changes are observed. In AsphF-T and AsphF/KOHs-T, the peak at 2922 cm^{-1} and 2847 cm^{-1} disappeared, likely due to thermal oxidation. AsphF/$Fe(NO_3)_3$s-T display additional peak at 835 cm^{-1} attributed to Fe–O stretching and nitrate group vibrations, confirming the incorporation of iron species.[33,34] These modifications also show a decrease in the intensity of the aliphatic C–H peaks, suggesting partial surface oxidation. Similarly, AsphF/$Al(NO_3)_3$s-T exhibit enhanced reduction in the intensity of the aromatic functional groups. These results confirm that chemical treatment introduces oxygen-containing and metal–oxygen functional groups while preserving the aromatic backbone of AsphF, which aligns with the gentle oxidizing nature of nitrate ions (NO_3^-) discussed earlier. Incorporating functional groups into the fibers while maintaining their structural integrity, ultimately increases the number of active binding sites.

The oxygen *versus* carbon composition of the untreated and chemically treated AsphF is given in Fig. 5. AsphF-T show no significant change in oxygen content, indicating a limited oxygenated functional group. In contrast, treatments with KOH, $Fe(NO_3)_3$s, and $Al(NO_3)_3$s result in a substantial reduction in carbon content relative to oxygen, suggesting successful surface functionalization through oxidation and/or formation of oxygenated species and metal complexes. This observation aligns with literature interpretation, where also the slight decrease in carbon content was attributed to partial oxidation.[25] This transformation is critical for the stabilization process as it facilitates the cross-linking of asphaltenes structures, pore creation, enhancing the thermal stability and structural integrity of the resulting carbon fibers.

3.2. Adsorption study

3.2.1. Adsorbent performance. MO adsorption by AsphF improves significantly with chemical modification, as shown in Fig. 6. AsphF and AsphF-T exhibited negligible adsorption capacity and removal efficiency, suggesting that the none chemically modified fibers have limited active sites for MO adsorption. In contrast, for AsphF/KOHs-T, AsphF/$Fe(NO_3)_3$s-T and AsphF/$Al(NO_3)_3$s-T the adsorption capacity and removal percentage increased, demonstrating the role of surface functionalization and increased porosity. Notably, AsphF/$Al(NO_3)_3$s-T achieved the highest removal efficiency (~43%) and adsorption capacity of approximately 3.2 mg g^{-1}, highlighting the superior effect of $Al(NO_3)_3$. Due to its outstanding adsorption performance, AsphF/$Al(NO_3)_3$s-T was selected for further in-depth studies, including the evaluation of adsorption isotherms, kinetics, thermodynamics, reusability, and potential for wastewater treatment.

3.2.2. Adsorption kinetics. The kinetics of MO adsorption onto AsphF/$Al(NO_3)_3$s-T were evaluated using five widely applied models: pseudo-first-order (PFO), pseudo-second-order (PSO), Elovich model, intraparticle diffusion and Bangham model to describe the adsorption mechanism and the rate-controlling steps.[22] Detailed fitting of the different models to the kinetic data of MO adsorption onto AsphF/$Al(NO_3)_3$s-T can be found in the ESI.†

Generally, PSO displayed a higher correlation coefficient (R^2 ~ 0.9830) across all concentrations (Table S1 and Fig. S6†) compared to the other models. PSO assumes chemical interactions, *via* electron transfer or valency forces, govern the rate of adsorption. It is noted that the adsorption of MO on different

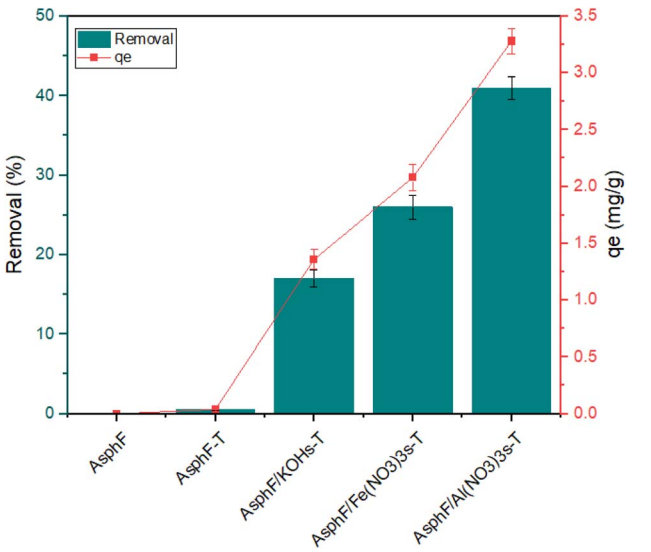

Fig. 6 Adsorption onto untreated and chemically treated AsphF: pH = 7, 298 K, 24 h, 200 rpm, C_i = 20 mg L^{-1} and 2.5 g adsorbent per L.

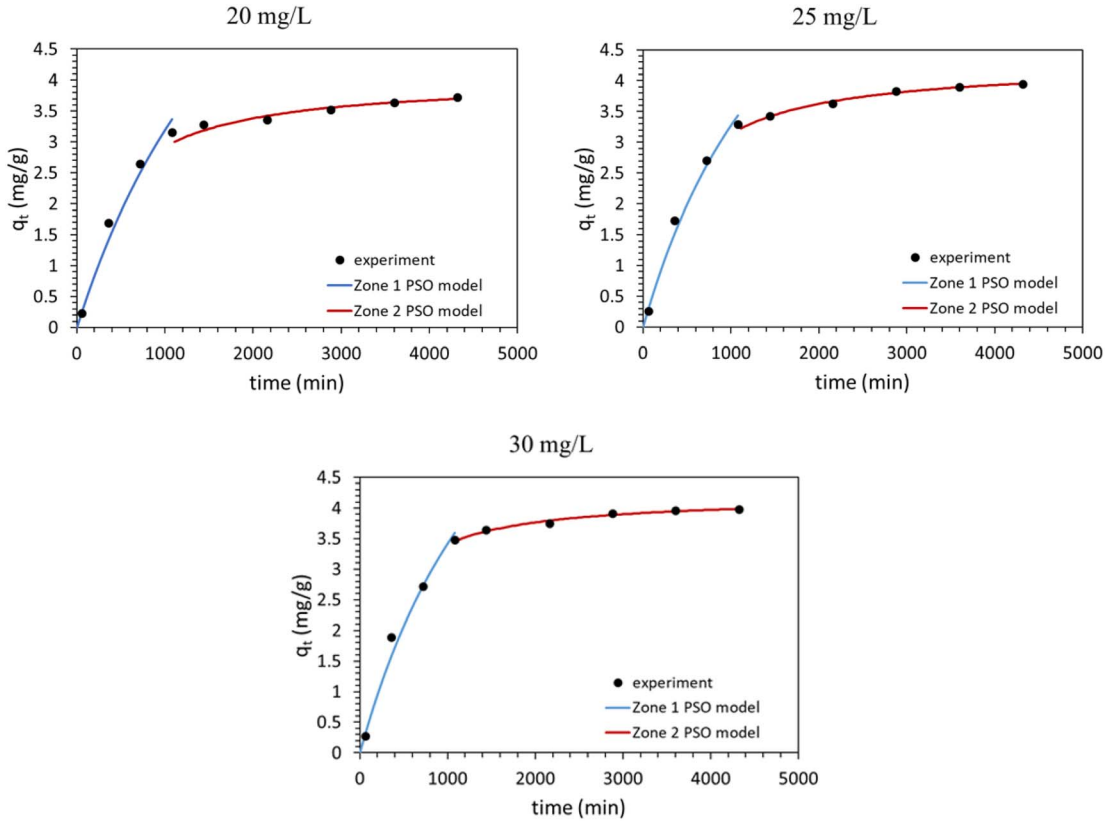

Fig. 7 PSO model for AsphF/Al$(NO_3)_3$s-T for different C_i.

adsorbents has been previously described using PSO kinetics.[3,23,35] Nevertheless, a closer look at MO adsorption data for the different initial concentrations reveals two distinct adsorption zones; $t \leq 18$ h (zone 1) and $t \geq 18$ h (zone 2). Fig. 7 and Table 4 show R^2 based on the linearized form of PSO for the two zones for different MO initial concentrations. For example, for 20 mg L^{-1} initial concentration of MO, the first zone exhibits low R^2 value (~0.5970), whereas the second zone displays high R^2 value (~0.9987). To thoroughly investigate these zones, Weber and Morris intraparticle diffusion model was applied.[36] The intraparticle diffusion model (Fig. 8) was fitted to the two adsorption zones. The fit appears excellent for the two zones ($R^2 \geq 0.9488$). Physically, zone 1 describes diffusion into mesopores. As evidenced by the higher $k_{i,1}$ value and negative intercept, I, the initial adsorption into mesopores represents rapid molecular diffusion into the larger pores. Conversely, zone 2 describes diffusion into micropores, as reflected by lower $k_{i,2}$ value and positive I. It is noted that zone 2 could be equally described by the pore diffusion model and the chemisorption model, which suggests diffusion into micropore or chemisorption mechanism.[2,22,36–38]

3.2.3. Adsorption isotherms. Several adsorption isotherms, including Langmuir, Freundlich, Temkin and Dubinin–Radushkevich (D–R), were fit to the equilibrium uptake for different C_i and temperatures, as shown in Fig. S10–S14.† Langmuir isotherm (Fig. 9), which assumes monolayer

Table 4 Parameters of the best fit kinetic model (PSO and intraparticle diffusion)

	Zone 1			Zone 2		
	20 mg L^{-1}	25 mg L^{-1}	30 mg L^{-1}	20 mg L^{-1}	25 mg L^{-1}	30 mg L^{-1}
PSO						
R^2	0.5970	0.8035	0.7554	0.9987	0.9997	0.9997
$q_{e\text{-}c}$ (mg g^{-1})	10.67	9.24	9.75	4.02	4.29	4.20
k_2 (g mg^{-1} min^{-1})		0.00005			0.00075	
Intraparticle diffusion						
R^2	0.9940	0.9967	0.9959	0.9831	0.9492	0.9488
I (mg g^{-1})	−0.621	−0.630	−0.645	2.623	2.731	3.166
k_i (g mg^{-1} $min^{-0.5}$)		0.122			0.016	

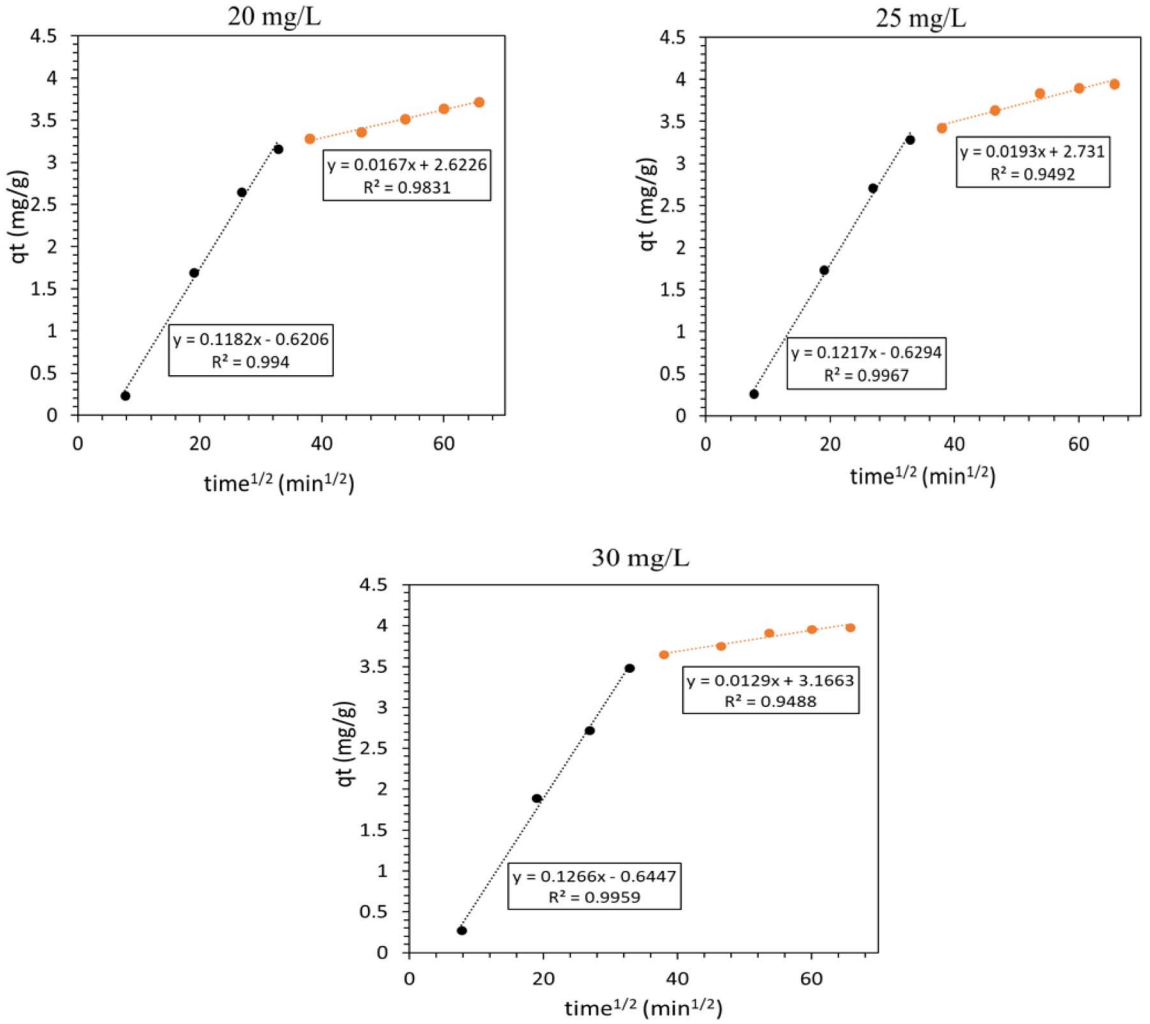

Fig. 8 Intraparticle diffusion model for AsphF/Al$(NO_3)_3$s-T for different C_i.

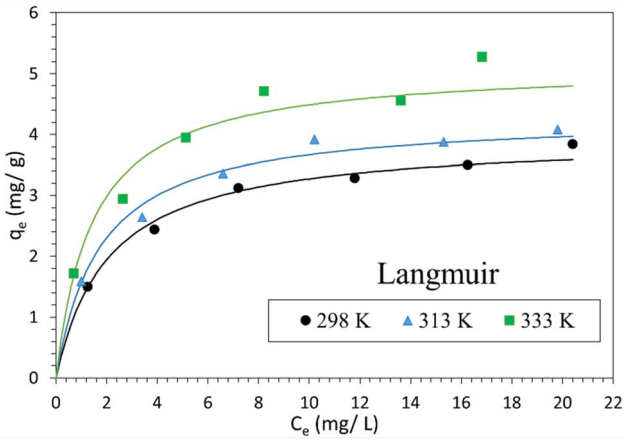

Fig. 9 Langmuir isotherms fit for uptake by AsphF/Al$(NO_3)_3$s-T at different temperatures.

adsorption onto a homogeneous surface with finite adsorption sites, displayed the best fit ($R^2 > 0.9782$) across all temperatures (Table S2†).

As the temperature increased from 298 K to 333 K, the adsorption capacity of the maximum uptake ($q_{max\text{-}L}$) also increased from 3.95 mg g^{-1} to 5.14 mg g^{-1}. The thermodynamic analysis discussed in the next section shows a positive ΔH^0 value, indicating an endothermic reaction that further supports a shift of the equilibrium toward more adsorption at higher temperatures. The separation factor (R_L) values extracted from Langmuir isotherm (Table 5), decreased from 0.09 to 0.07 with increasing temperature while $0 < R_L < 1$, which imply favorable adsorption of MO onto the AsphF/Al$(NO_3)_3$s-T adsorbent surface.[23]

3.2.4. Adsorption thermodynamics. Thermodynamics analysis is extremely important to study the heat interaction, spontaneity and feasibility of adsorption onto the surface of adsorbent. Thermodynamics parameters, including ΔH^0 and ΔS^0, can be evaluated using van't Hoff equation (eqn (18)). A plot of van't Hoff equation is presented in Fig. S15.† ΔG^0 values were subsequently calculated using eqn (20) at different temperatures.

The calculated values of ΔH^0, ΔS^0 and ΔG^0 in Table 6 provide valuable insight into the adsorption of MO onto AsphF/

Table 5 Langmuir isotherm parameter fit

	298 K	313 K	333 K
R^2	0.9917	0.9893	0.9782
$q_{max\text{-}L}$ (mg g^{-1})	3.95	4.31	5.14
K_L (L mg^{-1})	0.48	0.57	0.69
R_L	0.09	0.08	0.07

Table 6 Thermodynamic parameters for the adsorption of MO dye onto AsphF/Al$(NO_3)_3$s-T

T (K)	ΔG^0 (kJ mol^{-1})	ΔH^0 (kJ mol^{-1})	ΔS^0 (kJ K^{-1} mol^{-1})	R^2
298	−29.65	8.41	0.13	0.9995
313	−31.59			
333	−34.13			

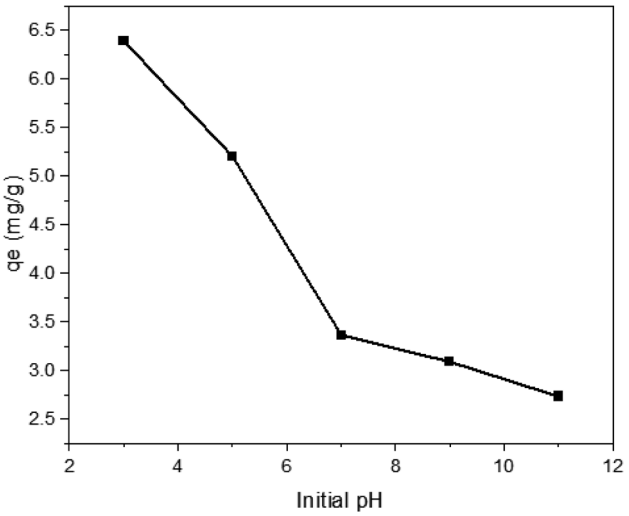

Fig. 10 pH effect on the adsorption of MO (298 K, 24 h, 200 rpm, C_i = 20 mg L^{-1}, 2.5 g adsorbent per L).

Al$(NO_3)_3$s-T. As reported in the literature,[39] ΔG^0 values for physical adsorption typically range from −20 to 0 kJ mol^{-1}, while those for chemical adsorption are generally between −400 and −80 kJ mol^{-1}. Based on Table 6, ΔG^0 values ranged from −29.65 to −34.13 kJ mol^{-1}, suggesting that the adsorption process was not a single physical or chemical adsorption but features both. This finding aligns with the results from the kinetic model, which point to multiple mechanisms influencing the adsorption process. It suggests that the adsorption of MO on AsphF/Al$(NO_3)_3$s-T is more complex than the PSO model suggests, highlighting that chemisorption is not the only factor affecting the adsorption rate. The negative values of ΔG^0 indicate that the adsorption process is spontaneous and becomes more favorable at higher temperatures. While reflecting an endothermic adsorption process, the positive ΔH^0 value of 8.41 kJ mol^{-1}, in principle, contributes to more positive ΔG^0. The spontaneity of the adsorption process can be explained by the steps involved during adsorption. Specifically, water molecules initially adsorbed onto the surface must be desorbed before any MO dye molecules are adsorbed. Since desorption of water molecules is an endothermic reaction, and adsorption is typically exothermic, it appears that the heat absorbed during water desorption exceeds the heat released during dye adsorption. This results in an overall endothermic process. Additionally, the molar volume of water molecules is much smaller than that of MO dyes, meaning numerous water molecules must be displaced to accommodate a single dye molecule.[40] The positive entropy change indicates an increase in the overall randomness at the solid–liquid interface during adsorption. While adsorption decreases randomness by organizing dye molecules onto the adsorbent surface, desorption of water molecules increases the system disorder, which in turn dominates the overall change in entropy contributing positive ΔS^0. This results agree with results obtained by ref. 40.

3.2.5. Impact of pH. The solution pH plays a crucial role in dye adsorption from aqueous solutions. The pH of the solution influences the surface charge on the adsorbent as well as the ionization of MO molecules.[41] Fig. 10 shows that the adsorption of MO onto AsphF/Al$(NO_3)_3$s-T is significantly influenced by the pH of the solution. At lower pH, the uptake increases, peaking at 6.32 mg g^{-1} at pH = 3. This increase is largely due to the protonation of oxygen-containing functional groups on the surface of the modified AsphF. The protonation increases the positive charge density on the adsorbent surface, which in turn strengthens the electrostatic attraction between with the anionic sulfonate group (SO_3^-) on MO.[23] However, increasing the pH from 3 to 11 results in a 57% reduction in uptake. This decline is attributed in part to the decreased protonation of the adsorbent surface, subsequently decreased electrostatic interaction with the dye. Additionally, at higher pH, the increased concentration of OH^- can compete with MO molecules for the positively charged adsorption sites due to protonation of functional groups or metal functionalization.[42]

3.2.6. Adsorption mechanisms. The adsorption mechanism of MO onto AsphF/Al$(NO_3)_3$s-T shown in Fig. 11 involves a combination of electrostatic interactions, π–π interactions, hydrogen bonding, van der Waals forces, and pore-filling effects, which synergistically enhance the adsorption process. The electrostatic aspect of the adsorption was discussed while discussing the effect of pH. The π–π interaction between the aromatic structures of MO and the π-electron-rich surfaces of AsphF/Al$(NO_3)_3$s-T further enhance the adsorption. The other van der Waals forces play a supplementary role in stabilizing the interaction between the dye molecules and the adsorbent surface. Hydrogen bonding occurs between the hydroxyl groups on the adsorbent surface and the nitrogen or oxygen atoms in MO, contributing to the stability of the adsorption process.[43] The hierarchical structure of AsphF/Al$(NO_3)_3$s-T provides a high surface area and pore volume, facilitating the physical and chemical entrapment of MO molecules at the surface of the pores.

Although this study used pure methyl orange, the main adsorption mechanisms are expected to apply to other similar anionic dyes. Nevertheless, real wastewater may contain

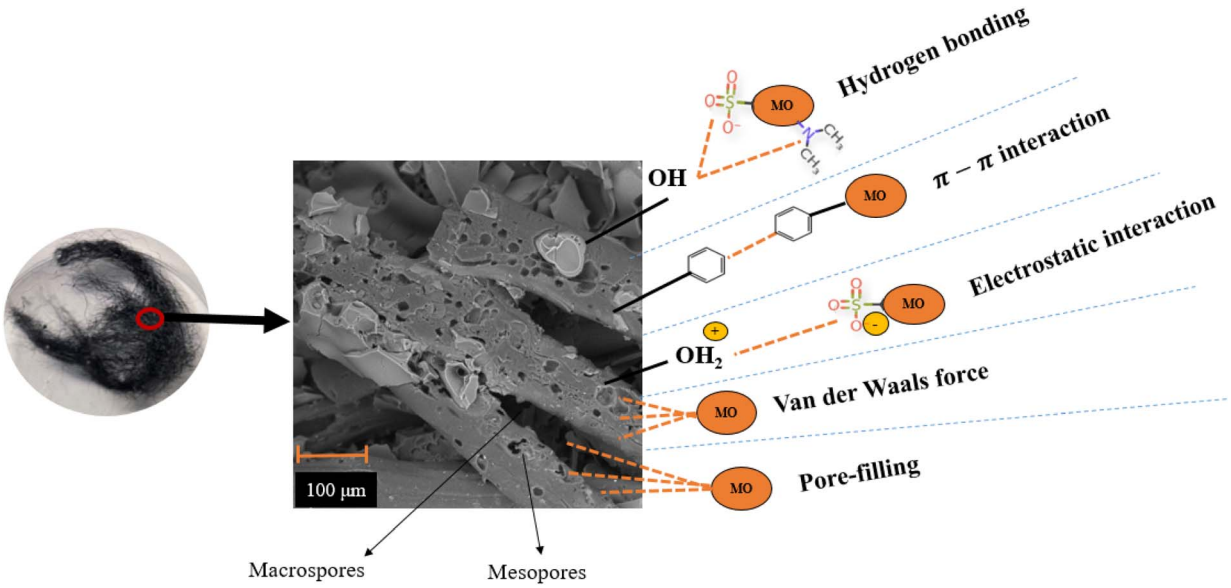

Fig. 11 Adsorption mechanisms of MO into AsphF/Al$(NO_3)_3$s-T. Note: micropores are not visible in this magnification.

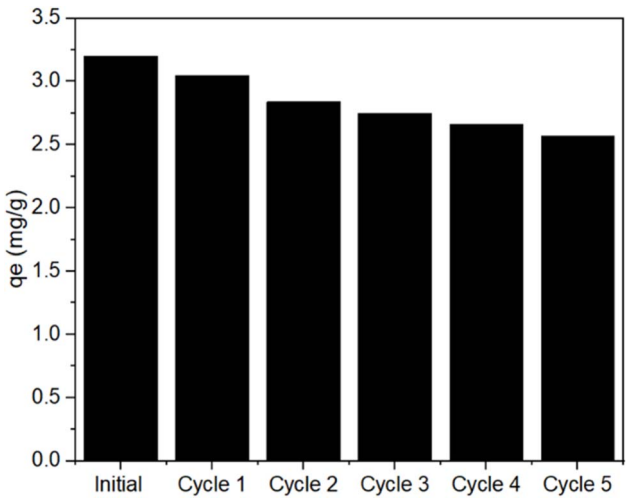

Fig. 12 Regeneration performance of AsphF/Al$(NO_3)_3$s-T toward MO adsorption experiments (298 K, 24 h, 200 rpm, $C_i = 20$ mg L^{-1}, 2.5 g adsorbent per L).

a combination of contaminants that may compete on adsorption sites, and/or alter the chemistry of a given contaminant, and/or adsorbent. Wastewaters belonging to certain industries may be considered in future work.

3.2.7. Regeneration of modified AsphF. The regeneration results of AsphF/Al$(NO_3)_3$s-T demonstrate its stability and reusability over multiple adsorption–desorption cycles as shown in Fig. 12. After the first cycle, a 8.54% decrease in adsorption capacity occurs, which continues to decline across the subsequent cycles. This reduction could be attributed to partial loss of surface functionality, irreversible adsorption of some MO molecules, or structural changes in the adsorbent during repeated cycles. However, the decline in performance remains minimal, with the adsorbent retaining a significant portion of its initial capacity, highlighting its practical potential for repeated use in wastewater treatment. These results underscore the adsorbent durability and efficiency for cyclic applications of dye removal from water.

The comparison of various adsorbents used for MO removal is shown in Table 7, highlighting their maximum uptake (q_{max}), pH conditions, and contact times. Among the adsorbents, AsphF/Al$(NO_3)_3$s-T from this study demonstrate a good adsorption capacity of 6.32 mg g^{-1} at pH = 3 with a contact time of 24 h.

Although the results are promising, there are some limitations to consider. The adsorption capacity of the modified fibers, while improved, is still lower than some advanced materials such as nanostructured adsorbents. In addition, the

Table 7 Summary of literature results on the adsorption of MO using different adsorbents at $T = 298$ K in comparison to current results

Adsorbent	q_{max} (mg g^{-1})	pH	Contact time	Reference
Chitosan beads	5.60	8	24 h	44
Functionalized multiwalled carbon nanotubes	52.86	2.3	2 h	45
Rice husk	1.30	2	35 min	46
Graphene oxide	16.83	3	100 min	47
Bottom ash	3.62	3	4 h	48
Modified asphaltenes particles	7.80	3	120 h	23
Modified asphaltenes fibers (AsphF/Al$(NO_3)_3$s-T)	6.32	3	24 h	This study

use of $Fe(NO_3)_3$, and $Al(NO_3)_3$ may lead to small amounts of metal leaching, which should be evaluated before applying the adsorbent on a larger scale. The experiments in this study were performed using a single dye under controlled conditions, but real wastewater usually contains a variety of contaminants that could affect adsorption. Moreover, while batch adsorption experiments do not capture the adsorbent performance in an industrial setting, column adsorption may be considered in a future study.

4. Conclusions

This study successfully developed hierarchical porous asphaltenes fibers chemically activated using KOH, $Fe(NO_3)_3$, and $Al(NO_3)_3$ *via* solid and impregnation mixing methods. Among the synthesized adsorbents, $Al(NO_3)_3$-modified asphaltenes fibers prepared through solid mixing exhibited the highest adsorption performance for MO dye, with a maximum uptake of 6.32 mg g^{-1} and 79% removal efficiency at pH = 3 and 298 K. The adsorption process followed the pseudo second order kinetic model and/or intraparticle diffusion. Initially, adsorption is driven by diffusion into mesopores, while in the second zone, it proceeds through either diffusion into micropores or chemisorption at active sites. Isotherm studies revealed that the Langmuir model best described the equilibrium uptake, confirming monolayer adsorption on a homogenous surface. Thermodynamic parameters demonstrated the endothermic and spontaneous nature of the adsorption, with positive entropy changes ($\Delta S^0 = 0.13$ kJ K^{-1} mol^{-1}) suggesting increased randomness at the solid–liquid interface. Regeneration experiments highlighted the adsorbent stability and reusability, with a 23.78% decline in adsorption capacity over five cycles. These findings underline the durability and cost-effectiveness of modified asphaltenes fibers.

Abbreviations

Symbol

AsphF	As-received asphaltenes fibers
AsphF-T	Heat treated asphaltenes fibers
AsphF/W-T	Heat treated impregnated asphaltenes fibers
AsphF/KOHs-T	Heat treated asphaltenes fibers solid mixed with KOH
AsphF/$Fe(NO_3)_3$s-T	Heat treated asphaltenes fibers solid mixed with $Fe(NO_3)_3$
AsphF/$Al(NO_3)_3$s-T	Heat treated asphaltenes fibers solid mixed with $Al(NO_3)_3$
AsphF/KOH_{aq}-T	Heat treated asphaltenes fibers impregnated with KOH
AsphF/$Fe(NO_3)_3$aq-T	Heat treated asphaltenes fibers impregnated with $Fe(NO_3)_3$
AsphF/$Al(NO_3)_3$aq-T	Heat treated asphaltenes fibers impregnated with $Al(NO_3)_3$
C_i	Initial concentration of MO (mg L^{-1})
C_t	Concentration of MO after a specific time (mg L^{-1})
C_e	Equilibrium MO concentration (mg L^{-1})
q_t	Adsorption uptake at a specific time (mg g^{-1})
q_e	Equilibrium adsorption capacity (mg g^{-1})
V	Volume of the solution containing the adsorbate (L)
m	Mass of the adsorbent used in the adsorption process (g)
k_1	Rate constant of the pseudo-first-order adsorption process (min^{-1})
k_2	Rate constant of the pseudo-second-order adsorption process (g mg^{-1} min^{-1})
k_i	Intraparticle diffusion rate constant (g mg^{-1} $min^{-0.5}$)
I	Intercept of the intraparticle diffusion model related to the boundary layer thickness (mg g^{-1})
k_0	Bangham constant (mL g^{-1} L^{-1})
$q_{max\text{-}L}$	Langmuir maximum adsorption uptake (mg g^{-1})
K_L	Langmuir isotherm constant (L mg^{-1})
R_L	Separation factor constant (unitless)
K_F	Freundlich isotherm constant (mg g^{-1} (L $mg^{-1})^{1/n}$)
$1/n$	Adsorption intensity factor (unitless)
B	Amount of adsorption heat (J mol^{-1})
A	Temkin equilibrium binding constant (L mg^{-1})
R	Universal gas constant 8.314 (J mol^{-1} K^{-1})
T	Absolute temperature (K)
$1/b_T$	Adsorption potential of adsorbent
$q_{max\text{-}D\text{–}R}$	Dubinin–Radushkevich maximum adsorption uptake (mg g^{-1})
E	Mean adsorption energy (J mol^{-1})
K	Thermodynamic equilibrium constant (unitless)
ΔS^0	Standard entropy change of the adsorption (J mol^{-1} K^{-1})
ΔH^0	Standard enthalpy change of the adsorption (J mol^{-1})
MW	Molar mass (g mol^{-1})
C^0	Standard concentration of the adsorbate (mol L^{-1})
ΔG^0	Standard Gibbs free energy change (J mol^{-1})

Greek symbol

$\alpha_{Elovich}$	Initial adsorption rate constant (mg g^{-1} min^{-1})
$\alpha_{Bangham}$	Constant in Bangham model (unitless)
$\beta_{Elovich}$	Desorption constant (g mg^{-1})
$\beta_{D\text{–}R}$	Activity coefficient related to adsorption mean free energy (mol^2 J^{-2})
ε	Constant related to Polanyi potential (J^2 mol^{-2})

Data availability

All data generated or analyzed during this study are either included in this published article or are available from the

corresponding author upon reasonable request. The core datasets supporting the adsorption experiments, material characterization (including FTIR spectra, BET surface area data, and SEM images), and kinetic and isotherm modeling results are available for academic and non-commercial use. Due to the file size and formatting of certain raw data outputs, they have not been uploaded publicly but can be shared in a suitable format upon request. Researchers interested in reproducing or further developing the study findings are encouraged to contact the corresponding author to obtain access to the original experimental datasets and supporting documentation.

Conflicts of interest

There are no conflicts to declare.

References

1 WHO, *WHO Global Water, Sanitation and Hygiene Annual Report 2019*, 2020.
2 K. Jedynak, M. Repelewicz, K. Kurdziel and D. Wideł, Mesoporous carbons as adsorbents to removal of methyl orange (Anionic dye) and methylene blue (cationic dye) from aqueous solutions, *Desalin. Water Treat.*, 2021, **220**, 363–379.
3 H. Alyasi, H. Mackey and G. McKay, Adsorption of Methyl Orange from Water Using Chitosan Bead-like Materials, *Molecules*, 2023, **28**, 6561.
4 W. Chen, X. Zhang, M. Mamadiev and Z. Wang, Sorption of perfluorooctane sulfonate and perfluorooctanoate on polyacrylonitrile fiber-derived activated carbon fibers: In comparison with activated carbon, *RSC Adv.*, 2017, **7**, 927–938.
5 S. Satyam and S. Patra, Innovations and challenges in adsorption-based wastewater remediation: A comprehensive review, *Heliyon*, 2024, **10**(9), e29573.
6 D. A. Gkika, A. C. Mitropoulos and G. Z. Kyzas, Why reuse spent adsorbents? The latest challenges and limitations, *Sci. Total Environ.*, 2022, **822**, 153612.
7 S. Fakher, M. Ahdaya, M. Elturki and A. Imqam, Critical review of asphaltene properties and factors impacting its stability in crude oil, *J. Pet. Explor. Prod. Technol.*, 2020, **10**, 1183–1200.
8 N. H. M. H. Tehrani, M. S. Alivand, D. M. Maklavany, A. Rashidi, M. Samipoorgiri, A. Seif and Z. Yousefian, Novel asphaltene-derived nanoporous carbon with N-S-rich micro-mesoporous structure for superior gas adsorption: Experimental and DFT study, *Chem. Eng. J.*, 2019, **358**, 1126–1138.
9 M. A. Rabeea, T. A. Zaidan, A. H. Ayfan and A. A. Younis, High porosity activated carbon synthesis using asphaltene particles, *Carbon Lett.*, 2020, **30**, 199–205.
10 O. Ioannidou and A. Zabaniotou, Agricultural residues as precursors for activated carbon production-A review, *Renewable Sustainable Energy Rev.*, 2007, **11**(9), 1966–2005.
11 K. Y. Foo and B. H. Hameed, Preparation and characterization of activated carbon from pistachio nut shells via microwave-induced chemical activation, *Biomass Bioenergy*, 2011, **35**(7), 3257–3261.
12 X. Zhang, L. Lin, W. Gao, Y. Zhou and Q. Lin, A novel Fe-containing carbon foam with hierarchical porous structure for efficient removal of organic dyes, *Diam. Relat. Mater.*, 2023, **140**, 110492.
13 S. Li, H. Zhang, S. Hu, J. Liu, Q. Zhu and S. Zhang, Synthesis of hierarchical porous carbon in molten salt and its application for dye adsorption, *Nanomaterials*, 2019, **9**(8), 1098.
14 A. K. Ishkildina and O. S. Travkina, Effects of the Method for the Preparation of Synthetic Aluminosilicate on the Properties of ZSM-5, *Pet. Chem.*, 2024, **64**, 181–185.
15 H. L. Girard, P. Bourrianne, D. Chen, A. Jaishankar, J. L. Vreeland, R. E. Cohen, K. K. Varanasi and G. H. McKinley, Asphaltene Adsorption on Functionalized Solids, *Langmuir*, 2020, **36**(14), 3894–3902.
16 S. Abedi, High performance electrode and catalyst nanomaterials for energy storage devices: Supercapacitors, pseudocapacitors and zinc-air batteries made from asphaltene based carbon fibers, PhD thesis, University of Alberta, 2023.
17 Sigma-Aldrich, *Potassium hydroxide, ACS reagent, ≥85%, pellets*, **https://www.sigmaaldrich.com/CA/en/product/sigald/221473**.
18 Sigma-Aldrich, *Iron(III) nitrate nonahydrate, ACS reagent, ≥98%*, **https://www.sigmaaldrich.com/US/en/product/sigald/216828**.
19 Sigma-Aldrich, *Aluminum nitrate nonahydrate, ACS reagent, ≥98%*, **https://www.sigmaaldrich.com/US/en/product/sigald/237973**.
20 A. G. De Crisci, R. Gieleciak, M. H. Mobarok, M. Ali, T. D. Ngo, K. Goswami, A. Khan and J. Chen, Producing asphaltene fibres from bitumen-derived asphaltenes for carbon fibre development: Part one–Electrospinning, *Can. J. Chem. Eng.*, 2023, **101**(5), 2633–2645.
21 M. A. Behnajady, N. Modirshahla and H. Fathi, Kinetics of decolorization of an azo dye in UV alone and UV/H2O2 processes, *J. Hazard. Mater.*, 2006, **136**(3), 816–821.
22 I. D. Mall, V. C. Srivastava and N. K. Agarwal, Removal of Orange-G and Methyl Violet dyes by adsorption onto bagasse fly ashdkinetic study and equilibrium isotherm analyses, *Dyes Pigm.*, 2006, **69**(3), 210–223.
23 A. Eshraghian, L. Yu, G. Achari and U. Sundararaj, Development of an effective asphaltene-derived adsorbent for wastewater treatment: Characterization and methyl orange removal study, *J. Environ. Chem. Eng.*, 2023, **11**(1), 109221.
24 X. Zhou, X. Yu, J. Hao and H. Liu, Comments on the calculation of the standard equilibrium constant using the Langmuir model in Journal of Hazardous Materials 422 (2022) 126863, *J. Hazard. Mater.*, 2022, **429**, 1–3.
25 D. Leistenschneider, P. Zuo, Y. Kim, Z. Abedi, D. G. Ivey, A. de Klerk, X. Zhang and W. Chen, A mechanism study of acid-assisted oxidative stabilization of asphaltene-derived carbon fibers, *Carbon Trends*, 2021, **5**, 100090.

26 E. De Rose, S. Bartucci, C. Poselle Bonaventura, G. Conte, R. G. Agostino and A. Policicchio, Effects of activation temperature and time on porosity features of activated carbons derived from lemon peel and preliminary hydrogen adsorption tests, *Colloids Surf., A*, 2023, **672**, 131727.

27 K. Phothong, C. Tangsathitkulchai and P. Lawtae, The analysis of pore development and formation of surface functional groups in bamboo-based activated carbon during co2 activation, *Molecules*, 2021, **26**(18), 5641.

28 I. Zojaji, A. Esfandiarian and J. Taheri-Shakib, Toward molecular characterization of asphaltene from different origins under different conditions by means of FT-IR spectroscopy, *Adv. Colloid Interface Sci.*, 2021, **289**, 102314.

29 X. Qiyong, K. Wyclif, P. Jingjun, R. Xiong, W. Deng, S. Zhang, J. Guo and Y. Yang, Analysis of Xinjiang asphaltenes using high precision spectroscopy, *RSC Adv.*, 2020, **10**(65), 39425–39433.

30 M. Alhreez and D. Wen, Molecular structure characterization of asphaltene in the presence of inhibitors with nanoemulsions, *RSC Adv.*, 2019, **9**(34), 19560–19570.

31 A. S. Shalygin, E. S. Milovanov, E. P. Kovalev, S. S. Yakushkin, S. G. Kazarian and O. N. Martyanov, In Situ FTIR Spectroscopic Imaging of Asphaltene Deposition from Crude Oil under n-Heptane and Acetone Flows, *Pet. Chem.*, 2022, **62**, 1087–1095.

32 W. T. Welch, R. R. Bledsoe, B. K. Wilt and M. B. Sumner, Process for analysis of asphaltene content in hydrocarbon mixtures by middle infrared spectroscopy, *US Pat.*, 6087662, filed May 22, 1998, and issued July 11, 2000.

33 S. F. Aval, A. Akbarzadeh, M. R. Yamchi, F. Zarghami, K. Nejati-Koshki and N. Zarghami, Gene silencing effect of SiRNA-magnetic modified with biodegradable copolymer nanoparticles on hTERT gene expression in lung cancer cell line, *Artif. Cells, Nanomed., Biotechnol.*, 2016, **44**, 188–193.

34 M. K. Trivedi and A. B. Dahryn Trivedi, Spectroscopic Characterization of Disodium Hydrogen Orthophosphate and Sodium Nitrate after Biofield Treatment, *J. Chromatogr. Sep. Tech.*, 2015, **6**(5), 1000282.

35 A. Abollé, K. Y. Urbain, K. Ollo, K. Y. Tchonrontcha and K. A. Rodrigue, Adsorption of Methyl Orange on Corncob Activated Carbon: Kinetic, Equilibrium, and Thermodynamic Studies, *Earthline J. Chem. Sci.*, 2022, **8**, 205–224.

36 C. Sutherland, A diffusion-chemisorption kinetic model for simulating biosorption using forest macro-fungus, fomes fasciatus, *International Research Journal of Plant Science*, 2010, **1**(4), 107–117.

37 N. K. Lazaridis and D. D. Asouhidou, Kinetics of sorptive removal of chromium(VI) from aqueous solutions by calcined Mg-Al-CO3 hydrotalcite, *Water Res.*, 2003, **37**(12), 2875–2882.

38 A. Pholosi, E. B. Naidoo and A. E. Ofomaja, Intraparticle diffusion of Cr(VI) through biomass and magnetite coated biomass: A comparative kinetic and diffusion study, *S. Afr. J. Chem. Eng.*, 2020, **32**, 39–55.

39 C. Li, Z. Xiong, J. Zhang and C. Wu, The Strengthening Role of the Amino Group in Metal-Organic Framework MIL-53 (Al) for Methylene Blue and Malachite Green Dye Adsorption, *J. Chem. Eng. Data*, 2015, **60**(11), 3414–3422.

40 S. Hussain, M. Kamran, S. A. Khan, K. Shaheen, Z. Shah, H. Suo, Q. Khan, A. B. Shah, W. U. Rehman, Y. O. Al-Ghamdi and U. Ghani, Adsorption, kinetics and thermodynamics studies of methyl orange dye sequestration through chitosan composites films, *Int. J. Biol. Macromol.*, 2021, **168**, 383–394.

41 Y. O. Khaniabadi, R. Heydari, H. Nourmoradi, H. Basiri and H. Basiri, Low-cost sorbent for the removal of aniline and methyl orange from liquid-phase: Aloe Vera leaves wastes, *J. Taiwan Inst. Chem. Eng.*, 2016, **68**, 90–98.

42 R. Lafi and A. Hafiane, Removal of methyl orange (MO) from aqueous solution using cationic surfactants modified coffee waste (MCWs), *J. Taiwan Inst. Chem. Eng.*, 2016, **58**(4), 424–433.

43 Y. S. Reddy, T. J. Jose, B. Dinesh, R. N. Kumar, P. S. Kumar and K. Kaviyarasu, Equilibrium, kinetic, and thermodynamic study of Direct Yellow 12 dye adsorption by biomass-derived porous graphitic activated carbon, *Biomass Convers. Biorefin.*, 2024, 6817–6833.

44 W. A. Morais, A. L. P. de Almeida, M. R. Pereira and J. L. C. Fonseca, Equilibrium and kinetic analysis of methyl orange sorption on chitosan spheres, *Carbohydr. Res.*, 2008, **343**(14), 2489–2493.

45 Y. Yao, H. Bing, X. Feifei and C. Xiaofeng, Equilibrium and kinetic studies of methyl orange adsorption on multiwalled carbon nanotubes, *Chem. Eng. J.*, 2011, **170**(1), 82–89.

46 D. R. Tchuifon, S. G. Anagho, E. Njanja, J. N. Ghogomu, N. G. Ndifor-Angwafor and T. Kamgaing, Equilibrium and kinetic modelling of methyl orange adsorption from aqueous solution using rice husk and egussi peeling, *Int. J. Chem. Sci.*, 2014, **12**(3), 741–761.

47 D. Robati, B. Mirza, M. Rajabi, O. Moradi, I. Tyagi, S. Agarwal and V. K. Gupta, Removal of hazardous dyes-BR 12 and methyl orange using graphene oxide as an adsorbent from aqueous phase, *Chem. Eng. J.*, 2016, **284**, 687–697.

48 A. Mittal, A. Malviya, D. Kaur, J. Mittal and L. Kurup, Studies on the adsorption kinetics and isotherms for the removal and recovery of Methyl Orange from wastewaters using waste materials, *J. Hazard. Mater.*, 2007, **148**(1–2), 229–240.